Unveiling Optical Properties in Underwater Images

Yael Bekerman, Shai Avidan and Tali Treibitz

Abstract—The appearance of underwater scenes is highly governed by the optical properties of the water (attenuation and scattering). However, most research effort in physics-based underwater image reconstruction methods is placed on devising image priors for estimating scene transmission, and less on estimating the optical properties. This limits the quality of the results. This work focuses on robust estimation of the water properties. First, as opposed to previous methods that used fixed values for attenuation, we estimate it from the color distribution in the image. Second, we estimate the veiling-light color from objects in the scene, contrary to looking at background pixels. We conduct an extensive qualitative and quantitative evaluation of our method vs. most recent methods on several datasets. As our estimation is more robust our method provides superior results including on challenging scenes.

Index Terms—Computational Photography, Image Restoration, Image Color Analysis

1 Introduction

PHYSICS-based single underwater image recovery is an ill-posed problem that is typically separated into two parts: estimating the water properties and using a prior to estimate transmission. Once these are estimated the scene is recovered. While there is substantial work about suitable priors, estimating water properties was relatively neglected. Nevertheless, these parameters have critical influence on the results. Here, we concentrate on robust estimation of these properties and show that this greatly improves results, especially for distant objects.

The water properties that control the scene appearance are attenuation and scattering. Attenuation coefficients control the exponential decay of light as a function of the traveled distance. The coefficients heavily depend on the wavelength [1]. However, so far, in single image methods this dependency has not been dealt with robustly. In haze this dependency is very small and can be ignored. Many underwater recovery methods stem from dehazing methods and thus often continue with this assumption. Others, that take into account the color dependency, use preset value(s) based on oceanographic measurements. However, it was recently shown [1] that using the oceanographic measurements per wavelength in wide-band color channels is erroneous as it does not take into account camera spectral sensitivity, etc. Therefore, here we present the first attempt to recover the coefficients directly from the image, without using preset values.

Scattering of light in the medium between the object and the camera introduces an additive component to the image. The further the object, there is more intervening medium and thus the scattering increases. The saturation value of this additive component is termed the veiling-light and it occurs when there are no objects in the line-of-sight (LOS). The veiling-light value is assumed constant across the scene and is usually estimated from visible areas in the image that contain no objects. This is not robust enough as often it is difficult to reliably find these areas due to low visibility. In addition, although the veiling-light is treated as a single global value in each scene, in reality it often exhibits non-uniformities. Here we still assume uniform illumination but do not estimate the veiling-light merely based on pixel appearance. Instead, we aim to estimate a robust value that fits the image formation model to the scene.

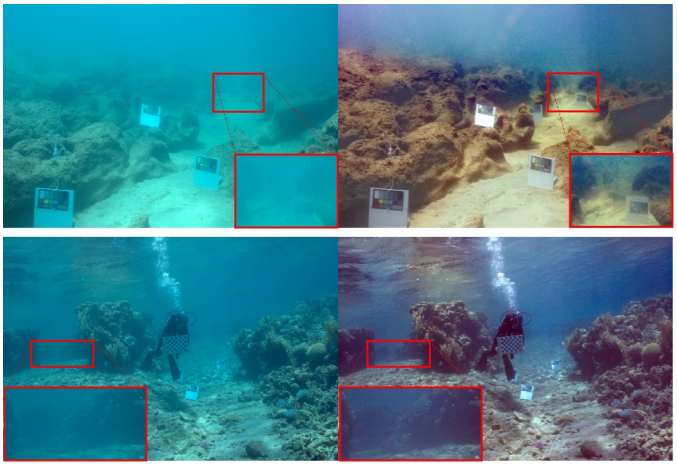

Fig. 1: [Left] Input underwater images. [Right] Results of our method. Note the recovery of very far objects, zoomed-in in the inserts.

Our key contribution is a method for estimating attenuation ratios and veiling light directly from the image. Once these ratios are estimated, we resort to a standard image dehazing algorithm to recover the full physical model of the scene that includes the transmission map, depth map, veiling light, and the clear image. Fig. 1 shows two examples underwater scenes and the results of our proposed method.

Recovering nearby objects in underwater images is rela-

- *Y. Bekerman and S. Avidan are with the School of Electrical Engineering, Tel Aviv University, Israel.*
- *T. Treibitz is with the School of Marine Sciences, University of Haifa, Israel.*
  E-mail: ttreibitz@univ.haifa.ac.il

tively easy and often a simple contrast stretch does the job. The problem becomes more challenging when the objects are farther away. This is where differences between methods are more pronounced. Therefore we evaluate our method on a recently released dataset that contains scenes with objects at the visibility limits. We show that our method provides superior reconstructions even in those challenging scenes, especially on the farthest objects. In addition, we provide an extensive comparison of very recent methods on this challenging dataset.

2 Related Work

We focus on reviewing most relevant underwater single image methods. We divide the relevant work into two categories. The first, image enhancement methods, that aim to enhance the appearance of the image without using any physical models. These methods do not reconstruct transmission maps. The second, physics-based image restoration methods, that aim to recover true color and transmission maps. As solving the image formation model is an under-constrained problem, these methods rely on image priors. The reader is referred to [2], [3], [4] for recent very comprehensive reviews of the growing body of research on this topic.

Image Enhancement. Image enhancement methods concentrate on increasing the contrast and correcting for color bias. They are mainly based on pixel intensity redistribution and expanding the dynamic range of the image histogram using one or several color models (such as RGB or HSV) [5], [6]. The most popular contrast enhancement methods used for underwater images are histogram equalization, contrast limited adaptive histogram equalization (CLAHE), gamma correction, white balancing and gray-world assumption. The most effective methods are fusion of these techniques [7], [8], [9], [10], [11].

Several deep learning methods were suggested for image enhancement, based either on end-to-end CNNs or on GANs. The training data used for the CNNs is either synthetic [12], [13] or based on results obtained from other underwater image enhancement methods [14], [15]. Both options for training are biased. GANs [16], [17], [18] have the advantage of not requiring pair-wise input-output training data that is very difficult to obtain. Therefore, they are used to transform the underwater images to look like in-air images using unorganized datasets of underwater images and in-air images.

Physics-Based Image Restoration. The dark channel prior (DCP) [19] assumes that most patches in natural images contain a very low intensity pixel in at least one color channel. Several methods used this prior or variants for underwater image enhancement [20], [21], [22], [23]. This prior was extensively verified for on-land images, but has limited applicability underwater, where ranges are much smaller and bright objects might occupy large portions of the field-of-view. Several underwater variants of it were suggested. UDCP [24], [25] omits the red channel, whereas the red channel prior [26] inverts it. Peng *et al*. [27] proposed a generalized dark channel prior (GDCP) based on the depth-dependent color by calculating the difference between the observed intensity and the background light.

Some methods use the per-patch difference between the red channel and the maximum between the blue and the green as a proxy for distance, termed the maximum intensity prior (MIP) by Carlevaris-Bianco *et al*. [28]. Li *et al*. [29] estimated the transmission based on it and then adjusted the contrast and brightness with histogram distribution. Song *et al*. [30] suggested the underwater light attenuation prior (ULAP) that assumes the object distance is linearly related to the difference between the red channel and the maximum blue-green. The blurriness prior [31] leverages the fact that images become blurrier with distance. Peng and Cosman [32] combined this prior with MIP and suggested the image blurring and light absorption (IBLA) prior.

The haze-lines prior (HL) [33] is based on the observation that the color intensity in natural images can be clustered to a small number of colors, and that under haze each cluster in the natural image becomes a line. Berman *et al*. [34] showed that the underwater image problem can be reduced to single image dehazing problem if the ratios of the attenuation coefficients are known. Based on the HL prior, Wang *et al*. [35] suggested the attenuation-curve prior, showing that color clusters in the natural image RGB plane become curves in the corresponding underwater RGB plane.

Deep networks that aim at physics-based restoration output an estimated transmission map, that is then used for restoration, rather than the restored image itself. For training they require datasets with pairs consisting of an underwater image and its ground-truth transmission. Such real-world datasets do not exist and therefore these methods rely on synthetic data for training [36], [37], [38], [39], [40]. This is problematic as the synthetic data usually does not encapsulate the entire complexity of the underwater realm. Li *et al*. [41] (waterGAN) trained their network using synthetic RGB-D underwater images generated using a GAN.

Water properties estimation. Physics-based method require estimation of the global veiling-light value and the water attenuation properties. Veiling-light is estimated as the brightest point (most methods based on DCP), using the farthest point [30], [32], or by finding a background textureless area that does not contain objects [25], [34]. Lu *et al*. [6] used the color lines prior [42] to estimate the veiling light assuming fixed attenuation (it cannot be done without this assumption). As opposed to these, our algorithm does not rely on background pixels for veiling-light estimation and finds a value that best fits the scene.

Estimating color-dependent attenuation is even more challenging. Some methods do not estimate the coefficients directly but perform some kind of a color-balance between the transmission channels [23]. Most methods assume preset fixed coefficients (usually ocean type I) [6], [22], [30], [32], [35]. The first attempt to estimate the coefficients was done by Berman *et al*. [34] who estimated two global attenuation coefficients ratios by iterating over ten water types defined by Jerlov [43]. The oceanographic measurements provide attenuation coefficients per wavelength. Previous methods that use preset values usually pick the measurement for each color channel from the peak wavelength of the camera sensitivity. It was shown in [44] that this is erroneous and that the color attenuation experienced by the wide-band color channels has different values that depend on the camera, etc. This is why it is important to estimate attenuation without

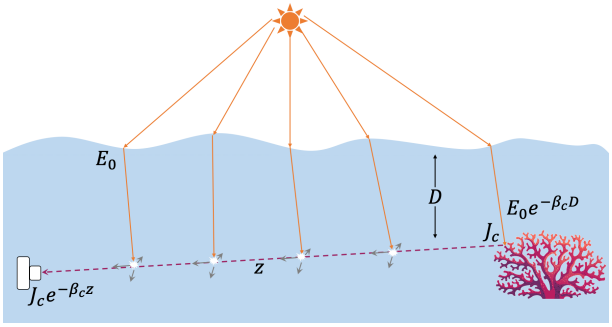

Fig. 2: Image formation model of a horizontal LOS. The sun's illumination is attenuated while it vertically propagates to the scene. Then, light reflected from the object is attenuated on its way to the sensor. Scattering from particles along the LOS contributes an additive component to the image intensity.

using preset types, as we firstly do here.

Revised underwater image formation model. It was shown recently [1], [44] that the image formation model used for underwater images in all the above methods leads to reconstruction errors as wavelength-dependent formulation cannot be directly transferred to a wide-band color space. The revised model has more parameters that when estimated using a known range-map were shown to result in superior reconstruction errors [45]. A single image method using the revised model has not been suggested yet as it has more parameters.

3 Background

3.1 Underwater Image Formation Model

The common underwater image formation [46] describes the underwater image intensity $I_c(\mathbf{x})$ at each pixel $\mathbf{x}$ and color channel $c \in \{R, G, B\}$ as follows

$$I_c(\mathbf{x}) = t_c(\mathbf{x})J_c(\mathbf{x}) + V_c(1 - t_c(\mathbf{x})) \quad . \tag{1}$$

where J_c is the object radiance, V_c is the veiling light, and t_c is the transmission coefficient. Vectors are denoted in **bold**.

The image signal I_c is an additive combination of the direct signal J_c and the veiling-light V_c which carries no information about the scene and therefore degrades the image. The object radiance J_c that we wish to restore is attenuated by the transmission t_c. The global veiling-light V_c is the image signal in areas that contain no objects. Note that since this is a physical model, the input image should be linear.

Assuming the water medium is homogeneous, the transmission is set by Bouguer's exponential law of attenuation, which is also known as the Beer-Lambert law [46]:

$$t_c(\mathbf{x}) = e^{-\beta_c z(\mathbf{x})} \quad , \tag{2}$$

where β_c is the water attenuation coefficient and it is color dependent. Here $z(\mathbf{x})$ is the distance along the line-of-sight (LOS) from the camera sensor to the scene at pixel $\mathbf{x}$ (see Fig. 2). The ratios between the attenuation coefficients are defined as:

$$\beta_{BR} = \frac{\beta_B}{\beta_R}, \quad \beta_{BG} = \frac{\beta_B}{\beta_G} \tag{3}$$

Similarly to horizontal attenuation described in Eq. (2), the vertical propagation of the light from the sea surface to the objects also induces attenuation that depends on the wavelength and the traveled distance. This is illustrated in Fig. 2. The incident illumination at the surface E_0 is attenuated with depth D, such that the incident illumination on the LOS is $E_c = E_0 e^{-\beta_c D}$. This results in an illumination color at depth that is different than the sun's illumination at the surface.

The image formation model in Eq. (1) assumes a horizontal LOS and that E_c is uniform in intensity and spectrum across the scene and the LOS, as the objects are located in approximately the same water depth. Thus, this illumination change can be viewed as a global color-cast in the scene.

The model in Eq. (1) is borrowed from haze and takes only horizontal effects into account. For our analysis we wish to separate the horizontal and vertical effects and therefore rewrite the equation to be

$$I_c(\mathbf{x}) = E_c t_c(\mathbf{x})\tilde{J}_c(\mathbf{x}) + E_c(1 - t_c(\mathbf{x})) \cdot \tilde{V}_c \quad . \tag{4}$$

So far methods that did not use the form of Eq. (4) actually estimated $E_c J_c$, and then compensated for E at the end of their algorithm pipeline by common global white-balance methods. This is physically true as E is a global effect.

However, we found that this cast has an effect on the performance of prior-based algorithms as they are based on natural images that do not have a strong color cast. Compensating for the global illumination first removes the color cast and aids the prior in identifying the distance-dependent effects better. Therefore, we conduct a simple global white balance by dividing the pixel values by the maximum in each channel *at the beginning of the process*. Then, from now on we assume the global color cast has been removed, i.e., $E_c = 1$, and concentrate on recovering the local distance-dependent effects.

3.2 Underwater Haze-Lines Prior-Based Method

The haze-lines prior [33] assumes that the colors in a clear image can be clustered to a final set of clusters, and shows that in hazy images these clusters become lines (termed *haze lines*) in RGB space in the form:

$$\mathbf{I}(\mathbf{x}) - \mathbf{V} = t(\mathbf{x})\left[\mathbf{J}(\mathbf{x}) - \mathbf{V}\right] \quad , \tag{5}$$

where in haze t is assumed to be uniform for all color channels, where $\mathbf{I}, \mathbf{J}, \mathbf{v}$ are spectral R,G,B vectors. Based on this observation they suggested a dehazing method that clusters the colors into lines after first estimating $\mathbf{V}$. The transmission per pixel is estimated from the value distribution along each haze-line.

Berman *et al.* [34] proposed a single image restoration of underwater scenes based on the haze lines prior. They showed that if the two global attenuation ratios $[\beta_{BR}, \beta_{BG}]$ are known, then Eq. (1) can be rewritten similarly to Eq. (5)

$$\begin{bmatrix} (I_R(\mathbf{x}) - V_R)^{\beta_{BR}} \\ (I_G(\mathbf{x}) - V_G)^{\beta_{BG}} \\ (I_B(\mathbf{x}) - V_B) \end{bmatrix} = t_B(x) \cdot \begin{bmatrix} (J_R(\mathbf{x}) - V_R)^{\beta_{BR}} \\ (J_G(\mathbf{x}) - V_G)^{\beta_{BG}} \\ (J_B(\mathbf{x}) - V_B) \end{bmatrix} \quad . \tag{6}$$

The form of Eq. (6) matches the image formation model for haze. Then, the haze-line prior [33] can be applied to

estimate t_B. Once t_B is evaluated, the image can be restored according to Eq. (6),

$$J_c(\mathbf{x}) = \frac{I_c(\mathbf{x}) - V_c}{t_B(\mathbf{x})^{\beta_c/\beta_B}} + V_c \quad . \tag{7}$$

In [34] $[\beta_{RB}, \beta_{GB}]$ were automatically chosen from a fixed set of options, that limited accuracy. In the following we show how to estimate them without aprioi knowledge.

4 Proposed Method

Given a linear underwater image we wish to restore the underlying scene to its true colors, i.e., as if there were no water between the camera and the scene. Based on Sec. 3 this requires estimation of the attenuation coefficients ratios $[\beta_{BR}, \beta_{BG}]$ and the veiling light $[V_R, V_G, V_B]$. The results of all prior-based methods are very sensitive to these values and therefore our method focuses on their robust estimation. Once they are estimated any prior can in theory be used for restoration. We use the haze-lines prior for recovery as its code easily adapts to our changes.

Our method is illustrated in Fig. 3 and summarized in Alg. 1. The code is available at: https://github.com/yaelbekerman/Unveiling-Optical-Properties.git. Next, we detail each stage.

Algorithm 1 Image Color Restoration

Input $\mathbf{I}(\mathbf{x})$ - linear image
Output $\mathbf{J}(\mathbf{x})$ - restored image, $t(\mathbf{x})$ - estimated transmission

1: Compensate for ambient illumination color $\forall c \in \{R, G, B\}$
2: Identify a textureless background area for initial veiling light estimation $\mathbf{V}$ and feasible range.
3: Calculate attenuation coefficients' ratios $[\beta_{BR}, \beta_{BG}]$ according to $\mathbf{V}$ using Eq. (8).
4: Find pixels with known ground-truth using a contrast enhanced image.
5: Solve for $\mathbf{V}$ using the GT pixels with Eq. (6) by nonlinear least-squares curve fitting minimization.
6: Calculate $[\beta_{BR}, \beta_{BG}]$ using $\mathbf{V}$.
7: Use Haze-Lines prior Eq. (7), with small modifications, to estimate an initial transmission t_B.
8: Regularize transmission using constrained WLS with lower bound constrains.
9: Calculate the restored image using Eq. (7).
10: Convert the restored linear image to sRGB image.

4.1 Estimating Ratios of Attenuation Coefficients

Contrary to previous methods [6], [22], [30], [32], [35] that used fixed sets of water types the power of our approach stems from estimating the attenuation coefficient ratios β_{BR}, β_{BG} directly from the image. This is significantly more accurate as it was shown in [44] that the coefficients depend on the camera sensitivity and other factors, and therefore using pre-defined values as done before results in errors.

Our approach (illustrated in Fig. 4) stems from Eq. (6). It was shown in [34] that color clusters in a clear image become curved lines in RGB space in underwater images and that knowing β_{BR}, β_{BG} can 'straighten' the curves. Thus, we look for the β_{BR}, β_{BG} values that give the best line approximation to the curves.

Mathematically, let us assume the veiling light $\mathbf{V}$ is known (we later detail how we estimate it). Denote $\mathbf{L} = \ln|\mathbf{I} - \mathbf{V}|$. Taking the log out of Eq. (6) and rewriting it, shows that $L_{c=R,G}$ is linearly related to L_B,

$$L_c = \beta_{Bc} L_B + \ln \frac{|J_c - V_c|}{|J_b - V_B|^{\beta_{Bc}}} \quad . \tag{8}$$

Interestingly, the slope of this line is the unknown β_{Bc}, *regardless* of the object color J_c that only affects the line intercept. We use this insight to estimate the coefficients directly out of the image without any a-priori data.

We do it as follows. First, we scatter plot the values of $L_{c=R,G}$ vs. L_B for all pixels in the image. Then we aim to find the line slopes that best fit the image data (separately for R and G). We consider the angles $\theta \in [20°, 70°]$. This range was chosen as it is physically feasible based on oceanographic data. For each θ we rotate the data, then divide the x axis into 500 bins. Each such bin represents a line with angle θ in the original data. We count the number of data points in each bin and average the top 10% bins with largest values. This average yields a score for each angle and the angle with the highest score is chosen separately in each of the BG, BR planes.

As can be seen in the results, this estimation yields robustness and the ability to better cope with farther objects. The algorithm steps are summarized in Alg. 2.

Algorithm 2 Attenuation Coefficients' Ratios Estimation

Input $\mathbf{I}(x)$ - linear image, $\mathbf{V}$ - veiling light
Output $[\beta_{BR}, \beta_{BG}]$ - attenuation coefficients' ratios

for $c = R, G$ **do**
  for $V \in \Omega_V$ **do**
    for each $\theta \in [20°, 70°], (u, v) \in (L_c, L_B)$ **do**
      $\begin{bmatrix} u' \\ v' \end{bmatrix} = \begin{bmatrix} \cos(\theta) & -\sin(\theta) \\ \sin(\theta) & \cos(\theta) \end{bmatrix} \times \begin{bmatrix} u \\ v \end{bmatrix}$
      divide values of u' into 500 bins
      bin_val = count in each bin
      $\theta_{\text{score}} = \text{mean}(\max 10\%(\text{bin\_val}))$
    $\tilde{\beta}_{Bc}[V] = \tan(\underset{\theta}{\text{argmax}}(\theta_{\text{score}}))$
  $\beta_{Bc} = \text{median}(\beta_{Bc})$

Implementation details. We assume that for small changes of the veiling light, the attenuation coefficients should not change. Therefore, in order to gain stability, we run this algorithm several times for values around $\mathbf{V}$, $\Omega_V = \{[V_c - 0.01 : 0.01 : V_c + 0.01]\}$ and get resulting coefficients $\Omega_{\beta_{cB}}$. We run the same algorithm on the GR plane and choose β_{BR}, β_{BG} from $\Omega_{\beta_{cB}}$ that minimize $\|\beta_{BR}/\beta_{BG} - \beta_{GR}\|$.

4.2 Veiling-Light Estimation

Estimating the veiling light correctly is important for solving the underwater image formation equation for any dehazing method. The image formation model Eq. (1) assumes a global veiling light for the entire image. However, very often this is not true– the sun is illuminating from an angle, etc. Therefore, methods that find the veiling light using

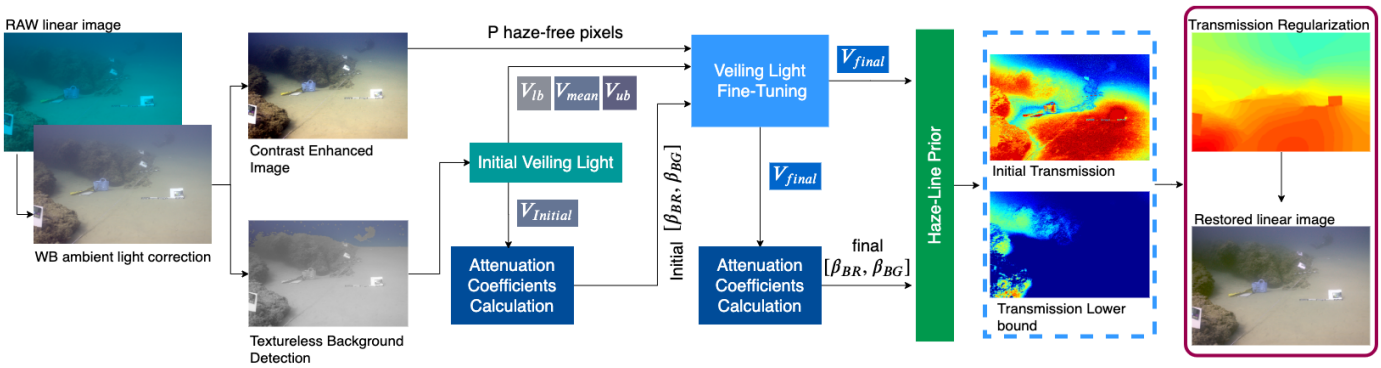

Fig. 3: The flow of our method.

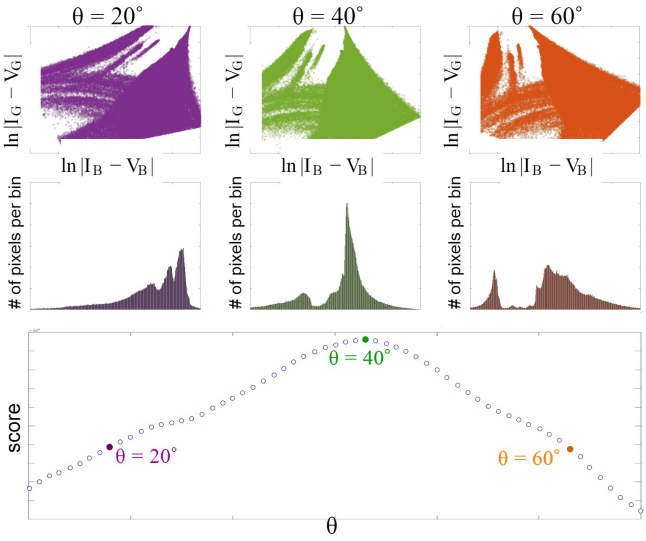

Fig. 4: Estimating attenuation coefficients. [Top] Data distribution in the $[\ln(I_B - V_B), \ln(I_G - V_G)]$ plane from image R3272, rotated by 3 different angles (20°, 40°, 60°). [Center] Number of data points for each x-axis value. [Bottom] The calculated score. The angle of $\theta = 40°$ receives the maximum score and therefore β_{BG} is set to $\tan(40°) = 0.84$.

background pixels from the scene are prone to instabilities. Moreover, due to low visibility, the background detection is sometimes erroneous (examples in Fig. 5), inserting errors into the process. To overcome these issues, we propose to find the veiling-light value that best fits the image formation model based on the given image.

We do this using the insight that a simple contrast stretch recovers the colors of the nearby pixels. These pixels are then used as pixels for which $\mathbf{J}$ is known. Using their values in Eq. (1) we find the missing $\mathbf{V}$ value using a nonlinear data-fitting minimization.

Finding Pixels with Known Ground-Truth. We perform a global contrast enhancement on the input image $\forall c \in \{R, G, B\}$:

$$I_c(\mathbf{x}) = \frac{I_c(\mathbf{x}) - \min(I_c)}{\max(I_c) - \min(I_c)} \quad . \tag{9}$$

Next we take the bottom third of the contrast-enhanced

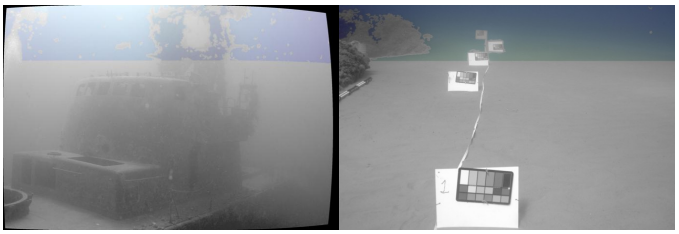

Fig. 5: Weak contrast in further areas sometimes results in errors when estimating veiling-light from a textureless background (indicated in blue). Note the wreck's bridge that was mistakenly marked as background (left) as well as the large sand area (right).

image, where we assume it is most likely to have nearby objects and cluster the image to P clusters according to intensity levels. For each cluster, each cluster center pixel $\hat{x}$ contributes a data pair for the minimization $[\mathbf{I}(\hat{x}), \mathbf{J}(\hat{x})]$.

Initial Guess And Boundary Conditions. Initial guess and boundary conditions are required for the two unknowns vectors - the veiling light $\mathbf{V}$ and the transmission for each cluster center $\mathbf{t}_B$. Note that $\mathbf{t}_B$ is solved for in the optimization but this value is not used afterwards.

The initial estimation for $\mathbf{V}$ is done by searching in the upper area of the image for a smooth area, without objects or texture, similarly to [34]. The pixels in this area are sorted according to their intensity. The pixel with the mean intensity provides the initial $\mathbf{V}$, the pixel at the 80% percentile the upper bound $\mathbf{V}_{\text{ub}}$, and the pixel at the 20% percentile the lower bound $\mathbf{V}_{\text{lb}}$. We use this guess to calculate β_{BR}, β_{BG} as explained in Sec. 4.1. For the transmissions the initial guess is set to be 0.9 as these are nearby objects, and the lower and upper bounds are set to be 0.7 and 1, respectively.

Final Veiling Light Estimation. We solve the following nonlinear least-squares problem with lower and upper bounds using an iterative curve fitting minimization optimization solver based on trust regions method [47],

$$\min_{\mathbf{V},\mathbf{t}_B} \sum_{p=1}^{P} \sum_{\substack{c \\ R,G,B}} \left\{ \beta_{Bc} \cdot \ln\left[\frac{V_c - I_c(p)}{V_B - J_B(i)}\right] - \ln\left(t_B(p)\right) \right\}^2 \tag{10}$$

$$s.t. \quad \mathbf{V}_{\text{lb}} \leqslant \mathbf{V} \leqslant \mathbf{V}_{\text{ub}}$$
$$0.7 \leqslant t_B \leqslant 1$$

In each iteration $\mathbf{V}$ is used for calculating β_{BR}, β_{BG} according to Sec. 4.1 and they are used for calculating the error. The resulting $\mathbf{V}$ is used to calculate the final β_{BG}, β_{BR} and together they are used for transmission estimation detailed next. The resulting values for t_B from Eq. (10) are ignored but when we examined them they were consistent with the assumptions.

4.3 Transmission Estimation and Regularization

We estimate the transmission based on the haze-line prior as described in [33], [34]. The estimated per-pixel transmission has to be regularized to enforce smoothness and overcome noise.

Contrary to Berman *et al*. [34] we use a constrained weighted linear least-squares problem using an interior-point method [48]. We set a lower bound on the transmission that stems from the constraint $J_c \geq 0$. In our experience this optimization together with the lower bound reduced artifacts and improved results.Since this optimization adds constraints per pixel, its run time is increased. To overcome this issue we down-sample the transmission map and iteratively up-sample it back, using the intensity guided depth up-sampling method in [49].

Finally, we convert the linear image to sRGB using a standard image processing pipeline [50].

5 Experimental Results

5.1 Datasets

We tested our algorithm on several datasets:
1. The dataset presented in [51] (available online [52]). This dataset contains 57 stereo images from four dive sites named *Nachsholim,Michmoret* (rocky reefs), *Satil* (a deep wreck) and *Katzaa* (coral reef). All the images are linear and were taken under natural light. The dataset enables a quantitative evaluation of restoration algorithms on natural images. For color comparison, color charts were placed at different distances from the camera. For transmission evaluation, ground truth distance maps were created using stereo imaging. Note that we used the stereo images and color charts for evaluation only. Our algorithm input was a single image with masked color charts.
2. Li *et al*. [53] collected 3800 underwater images from the internet and randomly selected 30 underwater images from their collected dataset for comparison.
3. Li *et al*. [15] collected 950 images from the internet, with different sizes and quality. They provide corresponding high-quality reference images to 890 images. The reference image was chosen from results of 12 different underwater image enhancement methods by 50 volunteers who performed pairwise comparisons among the 12 enhanced results.

Note that datasets **2** and **3** do not provide linear images required by our method. Yet, we are not aware of linear datasets other than **1** and use them to test our method on a variety of images.

5.2 Evaluated Methods

We set to conduct an extensive comparison of our method with most recent methods. For Li *et al*. [29] (MILP 2016) and Berman *et al*. [34] (UWHL 2017) we used official code provided online. Wang *et al*. [2] published code online for Li *et al*. [23] (GB UDCP 2016) and Song *et al*. [30] (ULAP 2018). Some authors sent us code in a private correspondence: Peng *et al*. [27], [32] (IBLA 2017, GDCP 2018), Wang *et al*. [35] (curve prior 2017) and Gao *et al*. [11] (local fusion 2019). Finally several authors sent us results on a subset of images through a private correspondence: Ancuti *et al*. [8], [9], [10] and Emberton *et al*. [25] .

Anwar and Li [4] conducted a comprehensive survey of latest deep underwater image enhancement networks [4], [15], [16], [17], [37], [53], tested on dataset 1 [51]. They concluded that in most cases, the deep learning-based methods fall behind state-of-the-art conventional methods as [34]. Therefore, we leave the reviewed methods in [4] out of the comparison here.

5.3 Qualitative Evaluations

Dataset 1. Fig. 6 presents a comparison on several images of methods we found are best performing, including zoom-ins to farther parts. A comparison of additional methods is presented in the supplementary. It can be seen that our results have better color and contrast than the others, including in farther parts as seen in the zoom-ins. The global contrast stretch gives overall visually pleasing results but as it is a global operation it does not recover distant areas (e.g. zoom-ins in #R3008, #R3204). Results of Ancuti *et al*. [10] are very detailed but with a color bias. This method also amplified the noise, especially in deep images with low signal (e.g., #R4388 zoom-in). Gao *et al*. [11] yields consistent decent results throughout the dataset but they tend to be grayish and over-saturated. This method also amplifies noise in dark areas (e.g, red artifacts in the deep dataset, bottom right of images #R4388, #R4366). Wang *et al*. [35] uses a fix set of β_{BR}, β_{BG} and therefore suffers from severe color skews. Berman *et al*. [34] choose β_{BR}, β_{BG} from a fixed set of 10 options which also results in color skew in #R4388 and pink halo in the farther areas in images #R3204, #R5478. All methods suffer from artifacts in dark places, as can be seen on the rocks and in #R4481 zoom-in. Our method avoids these artifacts, corrects the colors and recovers far objects.
Datasets 2 **and** 3**.** Our results on these datasets are presented in Figs. 7 and 8. These datasets are less suitable for our method as they do not provide linear images and not all images comply with our assumptions of ambient illumination in horizontal angle. Nevertheless, in dataset 2 our method still outperforms the best-ranking method presented in [53]. In dataset 3 in scenes under ambient illumination our results significantly improve on the reference image, especially in areas that are farther away from the camera.

5.4 Quantitative Evaluations

It is difficult to quantitatively evaluate underwater natural images. Unlike atmospheric dehazing, where natural image taken on a clear day can be ground truth to an hazy image taken on a foggy day, underwater images do not have a clear ground truth.

Some works use underwater image quality measures such as UCIQE and UIQM for evaluation. However, it was shown in Li *et al*. [53], that these measures sometimes

Fig. 6: Comparison of single-image underwater latest methods, with focus on interesting areas. Overall, the appearance of our results is the best, and especially in further areas, as seen at the bottom half of the page. Please zoom-in for better evaluation.

Fig. 7: Results on several images from dataset 2 [53]. Our results are compared to the results by [53], claimed to be best performing on this dataset. Our results have better color and contrast. Please zoom-in for better evaluation.

TABLE 1: Mean reproduction angular error $\overline{\Psi}$ of the gray patches in the color charts. Lower is better. Missing entries are due to the fact that the corresponding authors sent us results on specific images and not on the entire dataset.

Image	R3008	R5478	R4336	R3204	R4485	Nachsholim	Satil	Katzaa	Michmort	All
Contrast	10.88	**2.88**	6.54	10.54	7.88	11.47	7.20	8.14	4.88	7.57
Li 2016 [29]	12.20	17.12	29.00	10.62	14.46	11.77	29.13	19.19	18.62	18.68
Li 2016 [23]	17.00	21.64	35.31	22.76	28.06	23.58	35.15	28.48	26.39	27.53
Ancuti 2016 [8]	6.29	13.06	10.27	4.76	13.70					
Peng 2017 [32]	9.66	27.04	35.58	22.05	33.31	18.39	36.03	32.50	29.01	28.49
Peng 2018 [27]	14.97	26.66	35.68	24.44	34.66	22.89	35.78	33.27	32.01	30.79
Song 2018 [30]	16.83	32.08	36.04	28.88	37.26	22.30	36.44	35.42	30.84	30.88
Ancuti 2017 [9]	4.58	9.65	6.36	6.22	4.09					
Ancuti 2018 [10]	5.20	5.44	8.65	4.63	6.90					
Emberton 2018 [25]	6.70	36.15	35.75	8.61	36.40					
Wang 2018 [35]	10.20	23.46	35.47	26.45	36.82	16.84	35.90	35.28	26.70	28.00
Gao 2019 [11]	2.78	6.21	**6.73**	3.99	4.71	4.38	**6.10**	8.10	8.50	7.12
Berman 2017 [34]	4.68	4.75	33.47	2.73	9.40	7.28	25.48	8.88	6.68	10.03
Ours	**2.40**	4.47	8.41	**2.56**	**2.51**	**4.22**	11.27	**7.07**	**4.66**	**6.12**

give higher scores to results that are clearly wrong in the color (e.g., totally red). This happens as they are biased to specific image enhancement characteristics and do not take color shift and artifacts into account. Therefore, we use the quantitative evaluation on the ground truth measurements presented in [51], evaluation of color restoration on the color cards and evaluation of the transmission map vs. the stereo ground-truth.

The numerical evaluations are shown for each image that was presented visually in Fig. 6 and we also provide mean scores on the entire dataset, separated per dive site.

5.4.1 *Image Restoration Measures*

Color correction evaluation. To eliminate the influence of the global illumination, a median angle between the gray-scale patches and a pure gray color in sRGB space were calculated. We calculated the mean reproduction angular error $\overline{\Psi}$ on all the color charts in the image. The result is in degrees and lower angles indicate a more accurate color restoration. The sRGB space was used as most previous methods (except of [34]) output images in this space.

The results are summarized in Table 1. Some image enhancement methods [9]- [11] yield relatively low errors. Most physics-based methods yield very high errors, except of **our method that has the lowest errors** in 3 out of 4 dive sites and overall. Errors calculated on the color patches of the color charts and on just the farthest chart show a very similar trend, presented in the supplementary.

Transmission. The Pearson correlation coefficient (ρ) is used to calculate correlation between the ground-truth distance z and the estimated transmission $\tilde{z} = -\ln(t_c)$ (Eq. 2)

$$\rho = \frac{\mathrm{cov}(\tilde{z}, z)}{\sigma_{\tilde{z}} \sigma_z} \quad , \tag{11}$$

where cov is the covariance and $\sigma_{\tilde{z}}, \sigma_z$ are the standard deviations of $\tilde{z}, z$ respectively. The correlation coefficient has

TABLE 2: Pearson Correlation ρ: depth vs. -ln(transmission) calculated using Eq. (11). Missing entries are due to the fact that the corresponding authors sent us results on specific images and not on the entire dataset. As these are from the least performing methods this lack does not influence the evaluation.

Image	R3008	R4388	R5478	R4336	R3204	R4481	R4485	Nachsholim	Satil	Katzaa	Michmoret	All
Li 2016 [23]	0.36	0.51	-0.17	0.57	-0.08	0.07	0.37	0.31	0.35	0.19	-0.30	0.06
Ancuti 2016 [8]	0.08	0.12	-0.36	-0.22	-0.19	-0.03	-0.05					
Peng 2017 [32]	0.75	0.55	**0.82**	0.66	0.81	**0.68**	0.78	0.82	0.48	**0.72**	**0.87**	**0.76**
Peng 2018 [27]	0.11	0.43	-0.28	0.34	0.02	0.54	0.63	0.30	0.32	0.40	0.31	0.33
Song 2018 [30]	0.93	0.55	0.70	0.46	**0.94**	0.65	**0.82**	**0.90**	0.29	**0.72**	0.60	0.66
Emberton 2018 [25]	-0.17	0.28	-0.50	-0.42	-0.14	-0.47	0.13					
Berman 2017 [34]	0.78	0.50	0.64	0.49	0.86	0.09	0.73	0.84	0.37	0.66	0.73	0.68
Ours	**0.94**	**0.56**	**0.82**	**0.73**	0.90	0.14	0.82	0.84	**0.60**	0.63	0.77	0.72

Fig. 8: Results on several images from dataset 3 [15]. Our results are compared to the results that were selected the best among 50 volunteers. Our results present better contrast and color, especially in areas that are further away. Please zoom-in for better evaluation.

a value between -1 (opposite correlation) and $+1$ (perfect correlation).

The numerical results are presented in Table 2 and some scaled depth maps are shown in Fig. 9. It can be seen that our method yields a very good depth estimation, within the top 2 methods. In the challenging deep water dive site (the *Satil* dataset), where the colors in images are highly distorted, our method best restored the transmissions.

The prior-based methods that received the highest scores in depth estimation [30], [32], fail short in the color color correction evaluation (image results presented in the supplementary). We suspect this is because they used wrong values or image formation model for water properties.

5.5 Veiling light Estimation

As we do not have ground truth for $\mathbf{V}$, to assess its accuracy we examine whether the results are consistent, i.e., we expect to see clustering of the values according to dive site. Fig. 11 scatter plots the estimated veiling light $\mathbf{V}$ for each image in the dataset, colored by dive site. The values were normalized by intensity $(V_R + V_G + V_B)$ to ignore illumination changes and compare color. As can be seen in the graph, the values are approximately clustered with a linear discriminant analysis (LDA) score of 84.2%, demonstrating consistency of the estimation.

Now we examine the effect of the veiling light refinement stage in Eq. 10. The top row in Table 3 summarizes the ρ and $\overline{\Psi}$ score differences on dataset 1 when the refinement part is omitted, i.e., the initial guess is used as the veiling-light, similarly to previous methods. The refinement improves performance for most cases and without it the LDA score drops to 77.4%. Fig. 10 depicts an example. In this image the illumination is not uniform and therefore estimating $\mathbf{V}$ directly out of the image results in a bad transmission map and less correction of the farther parts (see for example the 3 top windows of the wreck). After the refinement stage the transmission is greatly improved, as well as the correction.

To examine the robustness of the veiling light step, we conducted a test where we perturbed the initial veiling light estimation to the lower and upper bounds $\mathbf{V}_{\text{lb}}, \mathbf{V}_{\text{ub}}$ of Eq. (10) that were often extremely different than the initial estimate. The lower and upper bounds were chosen as the minimum and maximum values in the entire background area and are often very dark ($\mathbf{V}_{\text{lb}}$) or very bright ($\mathbf{V}_{\text{ub}}$). With these values as an initial input the optimization in Eq. (10) did not converge to exactly the same veiling-light value, but the overall reconstruction results were very reasonable, as can be seen in Table 3.

5.6 Effect of White-Balancing in Pre-Processing

Here we demonstrate the effect of white-balancing the image before processing rather than at its end. The middle row in Table 3 summarizes the ρ and $\overline{\Psi}$ score differences on dataset 1 of our method when the white-balance is conducted as post-processing instead, as is often done. It can be seen that this seemingly innocent change has a significant positive effect on the results. Fig. 12 demonstrates this effect in a couple of examples.

To showcase the strength of our method we also tested the performance of Berman *et al*. [34] when its input was our white-balanced image (Table 3). Our results are much better and more robust, showing the effect of our method does not stem only from the pre-processing step.

6 Conclusions

Physics-based single image restoration methods require a good prior to recover a clean image, as well as an accurate

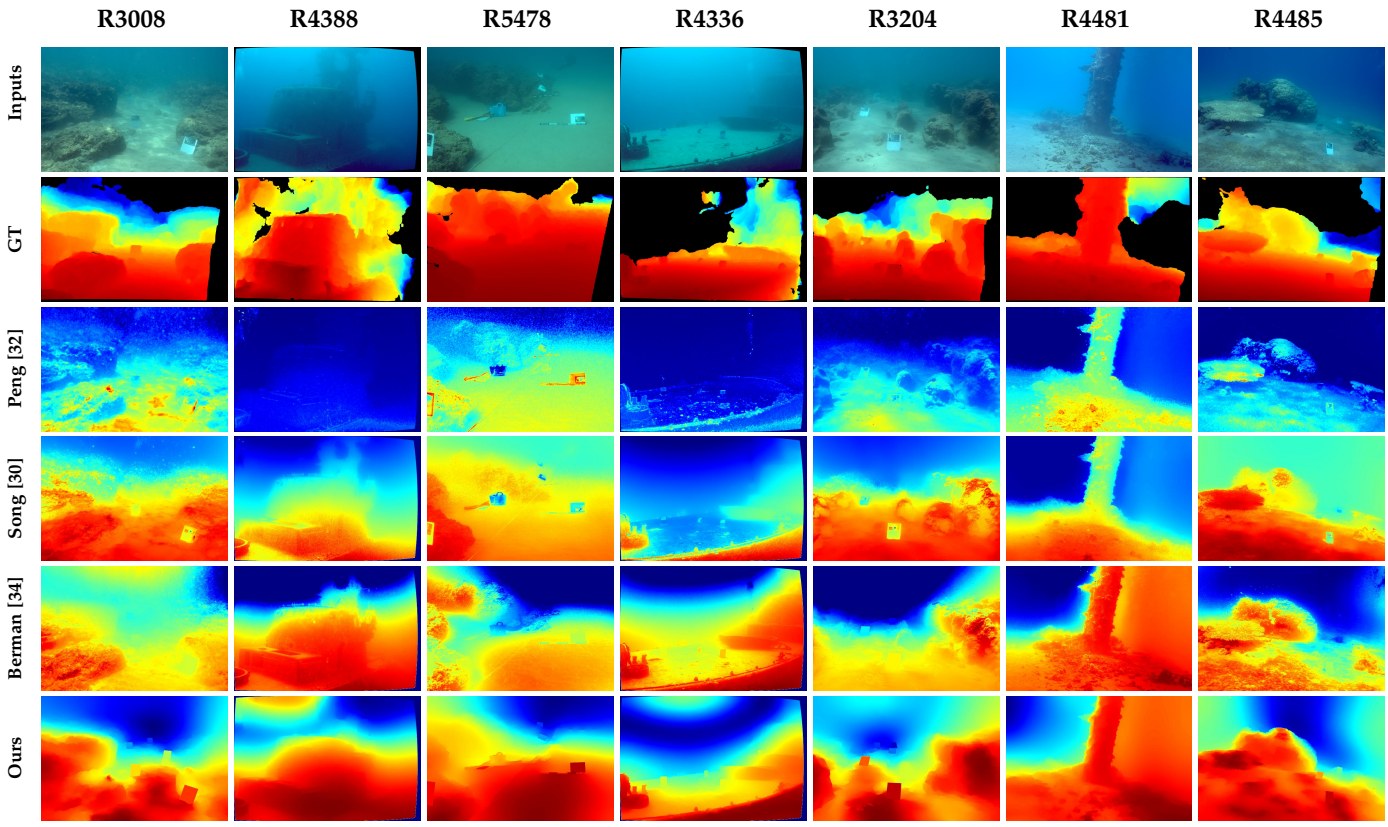

Fig. 9: Results of scaled depth estimation by the best performing methods.

TABLE 3: An ablation study of our method. The average transmission score ρ Eq. (11) and the scene restoration score $\overline{\Psi}$ are calculated per dive site for several variants of our method. First, using the initial estimation based on background pixels as veiling-light. Second and third, using lower and upper bounds as initial estimation for Eq. (10). Forth, white balancing the image in post-processing instead of pre-processing. Fifth, Berman *et al.* [34] with our pre-processed image as an input.

Method variant/Dive site	Nachsholim		Satil		Katzaa		Michmoret		All	
	ρ	$\overline{\Psi}$	ρ	$\overline{\Psi}$	ρ	$\overline{\Psi}$	ρ	$\overline{\Psi}$	ρ	$\overline{\Psi}$
No veiling light refinement	**0.84**	4.41	0.52	12.42	0.63	8.12	0.71	5.17	0.69	6.79
V_{lb} as initial guess for Eq. (10)	0.83	4.45	0.54	11.40	0.63	8.73	0.71	4.94	0.69	6.73
V_{ub} as initial guess for Eq. (10)	0.81	5.51	0.44	12.01	**0.66**	8.83	0.69	4.98	0.67	7.10
WB in post-processing	0.82	4.82	0.47	15.56	0.59	8.33	0.72	5.94	0.69	7.66
[34] with WB in pre-processing	0.81	8.72	0.41	14.37	0.53	8.00	0.70	6.06	0.64	8.35
Ours (full)	**0.84**	**4.22**	**0.60**	**11.27**	0.63	**7.07**	**0.77**	**4.66**	**0.72**	**6.12**

estimation of the water optical parameters. While there has been a considerable amount of work on new priors and methods for underwater image restoration, there has been much less work on estimating the water attenuation properties from single images. Most methods simply assumed fixed or preset attenuation values, which limited their ability to recover scene properties.

We are the first, to the best of our knowledge, to demonstrate a single image method to robustly estimate attenuation parameters from the image itself, as well as the veiling-light. It was shown in [1], [44] that it is not possible to directly use attenuation coefficients from Jerlov's water types in broadband images. The Jerlov coefficients are measured per wavelength and their manifestation in broadband images depends on many factors such as object distance, reflectance, etc. Therefore, the β_c coefficients in Eq. (2) are not physical parameters and it is difficult to evaluate their recovery compared to the Jerlov water types. This is why our method has a major advantage compared to all previous methods- methods that are based on using specific values from the Jerlov water types have an inherent limit of accuracy as these numbers are usually not the actual numbers that should be used. The power of our method is that it finds the coefficients that explain the imaged scene in the best way without using preset values. It also should be noted that the veiling light value that we estimate best fits the scene and does not rely on finding background pixel values.

We then use the recovered attenuation parameters and veiling light with an existing image restoration algorithm and witness a considerable improvement in the quality of the results. We further conducted a rigorous evaluation on

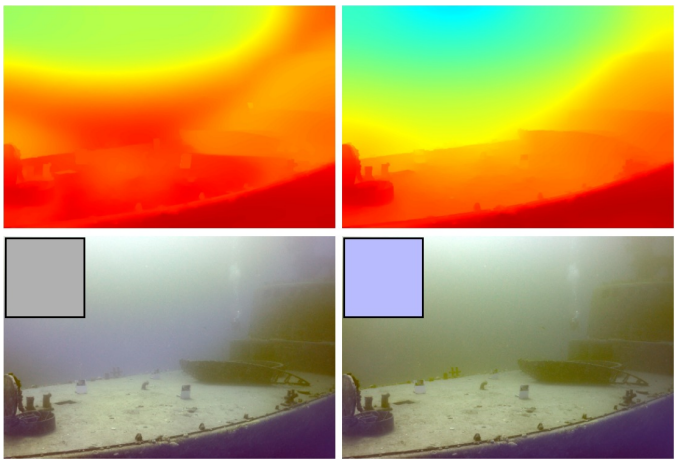

Fig. 10: The effect of the veiling light refinement (Eq. (10)), demonstrated on #R4336. [Right] Our method's results without the refinement. [Left] Results of our full pipeline. Transmission maps are at the top and restored scenes at the bottom, where the insert depicts the estimated $\mathbf{V}$. The refinement greatly improves the tranmission estimation and as a result the restored scene.

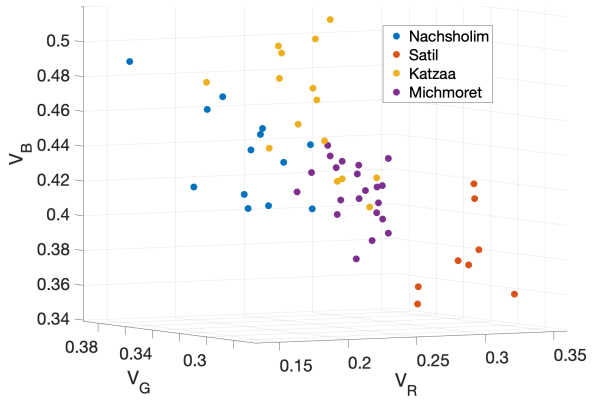

Fig. 11: Estimated veiling light $\mathbf{V}/(V_R + V_G + V_B)$ for each image, colored according to dive site to show consistency. Results show decent clustering, with an LDA score of 84.2%.

several datasets and show that our method performs the best in terms of scene restoration.

The parameter estimation method presented in this paper is independent of the restoration algorithm and can be used with other physics based image restoration algorithms.

Acknowledgements

TT was supported by the The Leona M. and Harry B. Helmsley Charitable Trust, The Maurice Hatter Foundation, Israel Science Foundation grant 680/18, and the Technion Ollendorff Minerva Center for Vision and Image Sciences. This work was also partly funded by ISF grant number 1549/19.

References

[1] D. Akkaynak and T. Treibitz, "A revised underwater image formation model," in *Proc. IEEE CVPR*, 2018, pp. 6723–6732.

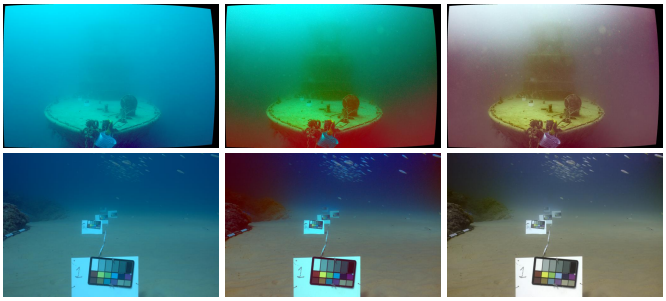

Fig. 12: The positive effect of white-balancing as a pre-processing step. [Left] Input. [Center] Our result with white-balance at post-processing. [Right] Our result with white-balance at pre-processing, as done in our method.

[2] Y. Wang, W. Song, G. Fortino, L.-Z. Qi, W. Zhang, and A. Liotta, "An experimental-based review of image enhancement and image restoration methods for underwater imaging," *IEEE Access*, vol. 7, pp. 140 233–140 251, 2019.
[3] M. Yang, J. Hu, C. Li, G. Rohde, Y. Du, and K. Hu, "An in-depth survey of underwater image enhancement and restoration," *IEEE Access*, vol. 7, pp. 123 638–123 657, 2019.
[4] S. Anwar and C. Li, "Diving deeper into underwater image enhancement: A survey," *arXiv preprint arXiv:1907.07863*, 2019.
[5] H. Lu, Y. Li, and S. Serikawa, "Underwater image enhancement using guided trigonometric bilateral filter and fast automatic color correction," in *Proc. IEEE ICIP*, 2013, pp. 3412–3416.
[6] H. Lu, Y. Li, L. Zhang, and S. Serikawa, "Contrast enhancement for images in turbid water," *JOSA A*, vol. 32, no. 5, pp. 886–893, 2015.
[7] C. Ancuti, C. O. Ancuti, T. Haber, and P. Bekaert, "Enhancing underwater images and videos by fusion," in *Proc. IEEE CVPR*. IEEE, 2012, pp. 81–88.
[8] C. Ancuti, C. O. Ancuti, C. De Vleeschouwer, R. Garcia, and A. C. Bovik, "Multi-scale underwater descattering," in *Proc. Int. Conf. Pattern Recognition (ICPR)*, 2016, pp. 4202–4207.
[9] C. O. Ancuti, C. Ancuti, C. De Vleeschouwer, L. Neumann, and R. Garcia, "Color transfer for underwater dehazing and depth estimation," in *Proc. IEEE ICIP*, 2017, pp. 695–699.
[10] C. O. Ancuti, C. Ancuti, C. De Vleeschouwer, and P. Bekaert, "Color balance and fusion for underwater image enhancement," *IEEE Trans. Image Processing*, vol. 27, no. 1, pp. 379–393, 2017.
[11] Y. Gao, J. Wang, H. Li, and L. Feng, "Underwater image enhancement and restoration based on local fusion," *J. of Electronic Imaging*, vol. 28, no. 4, p. 043014, 2019.
[12] Y. Wang, J. Zhang, Y. Cao, and Z. Wang, "A deep CNN method for underwater image enhancement," in *Proc. IEEE ICIP*, 2017.
[13] C. Li, S. Anwar, and F. Porikli, "Underwater scene prior inspired deep underwater image and video enhancement," *Pattern Recognition*, vol. 98, p. 107038, 2020.
[14] J. Perez, A. C. Attanasio, N. Nechyporenko, and P. J. Sanz, "A deep learning approach for underwater image enhancement," in *Int. Work-Conference on the Interplay Between Natural and Artificial Computation*. Springer, 2017, pp. 183–192.
[15] C. Li, C. Guo, W. Ren, R. Cong, J. Hou, S. Kwong, and D. Tao, "An underwater image enhancement benchmark dataset and beyond," *arXiv preprint arXiv:1901.05495*, 2019.
[16] Y. Guo, H. Li, and P. Zhuang, "Underwater image enhancement using a multiscale dense generative adversarial network," *IEEE J. of Oceanic Engineering*, 2019.
[17] J. Lu, N. Li, S. Zhang, Z. Yu, H. Zheng, and B. Zheng, "Multi-scale adversarial network for underwater image restoration," *Optics & Laser Technology*, vol. 110, pp. 105–113, 2019.
[18] J.-Y. Zhu, T. Park, P. Isola, and A. A. Efros, "Unpaired image-to-image translation using cycle-consistent adversarial networks," in *Proc. IEEE ICCV*, 2017, pp. 2223–2232.
[19] K. He, J. Sun, and X. Tang, "Single image haze removal using dark channel prior," *IEEE Trans. PAMI*, vol. 33, no. 12, pp. 2341–2353, 2010.
[20] L. Chao and M. Wang, "Removal of water scattering," in *Proc. Int. Conf. on Computer Engineering and Technology*, vol. 2, 2010, pp. V2–35.

[21] H.-Y. Yang, P.-Y. Chen, C.-C. Huang, Y.-Z. Zhuang, and Y.-H. Shiau, "Low complexity underwater image enhancement based on dark channel prior," in *Int. Conf. on Innovations in Bio-inspired Computing and Applications*, 2011, pp. 17–20.
[22] J. Y. Chiang and Y.-C. Chen, "Underwater image enhancement by wavelength compensation and dehazing," *IEEE Trans. Image Processing*, vol. 21, no. 4, pp. 1756–1769, 2011.
[23] C. Li, J. Quo, Y. Pang, S. Chen, and J. Wang, "Single underwater image restoration by blue-green channels dehazing and red channel correction," in *IEEE Int. Conf. on Acoustics, Speech and Signal Processing (ICASSP)*, 2016, pp. 1731–1735.
[24] P. Drews, E. Nascimento, F. Moraes, S. Botelho, and M. Campos, "Transmission estimation in underwater single images," in *Proc. IEEE CVPR workshops*, 2013, pp. 825–830.
[25] S. Emberton, L. Chittka, and A. Cavallaro, "Underwater image and video dehazing with pure haze region segmentation," *Computer Vision and Image Understanding*, vol. 168, pp. 145–156, 2018.
[26] A. Galdran, D. Pardo, A. Picón, and A. Alvarez-Gila, "Automatic red-channel underwater image restoration," *J. of Visual Communication and Image Representation*, vol. 26, pp. 132–145, 2015.
[27] Y.-T. Peng, K. Cao, and P. C. Cosman, "Generalization of the dark channel prior for single image restoration," *IEEE Trans. Image Processing*, vol. 27, no. 6, pp. 2856–2868, 2018.
[28] N. Carlevaris-Bianco, A. Mohan, and R. M. Eustice, "Initial results in underwater single image dehazing," in *Proc. MTS/IEEE OCEANS*, 2010.
[29] C. Li, J. Guo, S. Chen, Y. Tang, Y. Pang, and J. Wang, "Underwater image restoration based on minimum information loss principle and optical properties of underwater imaging," in *Proc. IEEE ICIP*, 2016, pp. 1993–1997.
[30] W. Song, Y. Wang, D. Huang, and D. Tjondronegoro, "A rapid scene depth estimation model based on underwater light attenuation prior for underwater image restoration," in *Pacific Rim Conference on Multimedia*. Springer, 2018, pp. 678–688.
[31] Y.-T. Peng, X. Zhao, and P. C. Cosman, "Single underwater image enhancement using depth estimation based on blurriness," in *Proc. IEEE ICIP*, 2015, pp. 4952–4956.
[32] Y.-T. Peng and P. C. Cosman, "Underwater image restoration based on image blurriness and light absorption," *IEEE Trans. Image Processing*, vol. 26, no. 4, pp. 1579–1594, 2017.
[33] D. Berman, S. Avidan *et al.*, "Non-local image dehazing," in *Proc. IEEE CVPR*, 2016, pp. 1674–1682.
[34] D. Berman, T. Treibitz, and S. Avidan, "Diving into haze-lines: Color restoration of underwater images," in *Proc. British Machine Vision Conference (BMVC)*, 2017.
[35] Y. Wang, H. Liu, and L.-P. Chau, "Single underwater image restoration using adaptive attenuation-curve prior," *IEEE Trans. Circuits and Systems I*, vol. 65, no. 3, pp. 992–1002, 2017.
[36] X. Ding, Y. Wang, J. Zhang, and X. Fu, "Underwater image dehaze using scene depth estimation with adaptive color correction," in *Proc. MTS/IEEE OCEANS*, 2017.
[37] M. Hou, R. Liu, X. Fan, and Z. Luo, "Joint residual learning for underwater image enhancement," in *Proc. IEEE ICIP*, 2018, pp. 4043–4047.
[38] K. Cao, Y.-T. Peng, and P. C. Cosman, "Underwater image restoration using deep networks to estimate background light and scene depth," in *Proc. IEEE Southwest Symposium on Image Analysis and Interpretation (SSIAI)*, 2018.
[39] W. V. Barbosa, H. G. Amaral, T. L. Rocha, and E. R. Nascimento, "Visual-quality-driven learning for underwater vision enhancement," in *Proc. IEEE ICIP*, 2018, pp. 3933–3937.
[40] Y. Hashisho, M. Albadawi, T. Krause, and U. F. von Lukas, "Underwater color restoration using u-net denoising autoencoder," *arXiv preprint arXiv:1905.09000*, 2019.
[41] J. Li, K. A. Skinner, R. M. Eustice, and M. Johnson-Roberson, "Watergan: Unsupervised generative network to enable real-time color correction of monocular underwater images," *IEEE Robotics and Automation letters*, vol. 3, no. 1, pp. 387–394, 2017.
[42] R. Fattal, "Dehazing using color-lines," *ACM Transactions on Graphics (TOG)*, vol. 34, no. 1, p. 13, 2014.
[43] N. Jerlov, "Marine optics, volume 14 of," *Oceanography*, 1976.
[44] D. Akkaynak, T. Treibitz, T. Shlesinger, Y. Loya, R. Tamir, and D. Iluz, "What is the space of attenuation coefficients in underwater computer vision?" in *Proc. IEEE CVPR*, 2017, pp. 4931–4940.
[45] D. Akkaynak and T. Treibitz, "Sea-thru: A method for removing water from underwater images," in *Proc. IEEE CVPR*, 2019, pp. 1682–1691.
[46] Y. Y. Schechner and N. Karpel, "Recovery of underwater visibility and structure by polarization analysis," *IEEE J. of Oceanic Engineering*, vol. 30, no. 3, pp. 570–587, 2005.
[47] T. F. Coleman and Y. Li, "An interior trust region approach for nonlinear minimization subject to bounds," *SIAM J. on optimization*, vol. 6, no. 2, pp. 418–445, 1996.
[48] A. Altman and J. Gondzio, "Regularized symmetric indefinite systems in interior point methods for linear and quadratic optimization," *Optimization Methods and Software*, vol. 11, no. 1-4, pp. 275–302, 1999.
[49] Y. Konno, Y. Monno, D. Kiku, M. Tanaka, and M. Okutomi, "Intensity guided depth upsampling by residual interpolation," in *The Abstracts of the international conference on advanced mechatronics: toward evolutionary fusion of IT and mechatronics: ICAM 2015.6*. The Japan Society of Mechanical Engineers, 2015, pp. 1–2.
[50] R. Sumner, "Processing raw images in matlab," 2014.
[51] D. Berman, D. Levy, S. Avidan, and T. Treibitz, "Underwater single image color restoration using haze-lines and a new quantitative dataset," *IEEE Transactions on Pattern Analysis and Machine Intelligence*, 2020.
[52] D. Berman, D. Levy, S. Avidan, and T. Treibitz, "Underwater single image quantitative dataset," http://csms.haifa.ac.il/profiles/tTreibitz/datasets/ambient_forwardlooking/index.html.
[53] C. Li, J. Guo, and C. Guo, "Emerging from water: Underwater image color correction based on weakly supervised color transfer," *IEEE Signal processing letters*, vol. 25, no. 3, pp. 323–327, 2018.

Yael Bekerman received her B.Sc. in Electrical Engineering from the Technion-Israel Institute of Technology in 2011 and her M.Sc. in Electrical Engineering from Tel Aviv University in 2020. Her research interests include computer vision and image processing with a focus on physics-based image restoration.

Shai Avidan received the PhD degree from the School of Computer Science, Hebrew University, Jerusalem, Israel, in 1999. He is currently a professor on the Faculty of Engineering, Tel Aviv University, Tel Aviv, Israel. In between, he worked for Adobe, Mitsubishi Electric Research Labs, and Microsoft Research. He has published extensively in the fields of object tracking in video and 3D object modeling from images. He is also interested in Internet vision applications such as privacy-preserving image analysis, distributed algorithms for image analysis, and image retargeting.

Tali Treibitz received her BA degree in Computer Science and her PhD degree in Electrical Engineering from the Technion-Israel Institute of Technology in 2001 and 2010, respectively. Between 2010-2013 she has been a post-doctoral researcher in the department of computer science and engineering, in the University of California, San Diego and in the Marine Physical Lab in Scripps Institution of Oceanography. Since 2014 she is heading the Marine Imaging Lab in the School of Marine Sciences in the University of Haifa. She was the recipient of the Google Anita Borg Scholarship in 2009 and the Weizmann Institute of Science National Postdoctoral Award for Advancing Women in Science in 2010.